AGU PUBLICATIONS

JGR

Journal of Geophysical Research: Atmospheres

RESEARCH ARTICLE

10.1002/2014JD021977

# Aerosol radiative forcing from the 2010 Eyjafjallajökull volcanic eruptions

**M. G. Flanner[1], A. S. Gardner[2], S. Eckhardt[3], A. Stohl[3], and J. Perket[1]**

[1]Department of Atmospheric, Oceanic, and Space Sciences, University of Michigan, Ann Arbor, Michigan, USA, [2]Graduate School of Geography, Clark University, Worcester, Massachusetts, USA, [3]Norwegian Institute for Air Research, Kjeller, Norway

**Key Points:**
- We derive aerosol radiative forcing from the 2010 eruptions of Eyjafjallajokull
- Sulfate cooling was nearly offset by ash longwave and in-snow shortwave heating
- We cannot rule out positive net forcing because of uncertainty in ash properties

**Supporting Information:**
- Readme
- Table S1
- Table S2
- Table S3
- Table S4
- Table S5
- Table S6
- Data S1
- Animation S1

**Correspondence to:**
M. G. Flanner,
flanner@umich.edu

**Citation:**
Flanner, M. G., A. S. Gardner, S. Eckhardt, A. Stohl, and J. Perket (2014), Aerosol radiative forcing from the 2010 Eyjafjallajökull volcanic eruptions, *J. Geophys. Res. Atmos.*, *119*, 9481–9491, doi:10.1002/2014JD021977.

Received 30 APR 2014
Accepted 21 JUL 2014
Accepted article online 24 JUL 2014
Published online 6 AUG 2014

**Abstract** Although the 2010 volcanic eruptions of Eyjafjallajökull did not exert a large climate forcing, several features of their emissions favored weaker aerosol cooling or stronger warming than commonly attributed to volcanic events. These features include a high ratio of fine ash to $SO_2$, occurrence near reflective surfaces exposed to strong insolation, and the production of very little stratospheric sulfate. We derive plausible ranges of optical properties and top-of-atmosphere direct radiative forcing for aerosol emissions from these events and find that shortwave cooling from sulfate was largely offset by warming from ash deposition to cryospheric surfaces and longwave warming from atmospheric ash and sulfate. Shortwave forcing from atmospheric ash was slightly negative in the global mean under central estimates of optical properties, though this forcing term was uniquely sensitive to the simulated distribution of clouds. The forcing components sum to near climate-neutral global mean 2010 instantaneous ($-1.9$ mW m$^{-2}$) and effective ($-0.5$ mW m$^{-2}$) radiative forcing, where the latter is elevated by high efficacy of snow-deposited ash. Ranges in net instantaneous ($-7.3$ to $+2.8$ mW m$^{-2}$) and effective ($-7.2$ to $+4.9$ mW m$^{-2}$) forcing derived from sensitivity studies are dominated by uncertainty in ash shortwave absorptivity. Forcing from airborne ash decayed quickly, while sulfate forcing persisted for several weeks and ash deposits continued to darken snow and sea ice surfaces for months following the eruption. Despite small global forcing, monthly averaged net forcing exceeded 1 W m$^{-2}$ in some regions. These findings indicate that ash can be an important component of climate forcing from high-latitude volcanic eruptions and in some circumstances may exceed sulfate forcing.

## 1. Introduction

Impacts of volcanic aerosol emissions on climate have been widely studied [e.g., *Robock*, 2000]. Major volcanic eruptions cool global climate through production of sulfate aerosol in the stratosphere, which can increase the albedo of the planet for years following the eruption. Ash injections can exert positive direct top-of-atmosphere radiative forcing when lofted over surfaces of high albedo [e.g., *Young et al.*, 2012] but tend to be shorter lived because the particles are much larger than sulfate. Ash deposits can also accelerate snow melt [*Conway et al.*, 1996] and may have contributed to Snowball Earth deglaciation [*Le Hir et al.*, 2010; *Abbot and Pierrehumbert*, 2010], but radiative forcings associated with this aspect of volcanic activity have not been quantified. The eruptions of Iceland's Eyjafjallajökull (63.6°N, 19.6°W) during April–May 2010 gained notoriety for disrupting European air traffic, but their climate forcing has yet to be quantified. Although climate impacts from these events were undoubtedly small in comparison with eruptions like that of Mount Pinatubo in 1991 [*Robock*, 2013], Eyjafjallajökull emissions exhibited several characteristics that help offset the cooling from its $SO_2$ emissions, including a large emission ratio of fine ash [e.g., *Gudmundsson et al.*, 2012], which absorbs a much higher proportion of incident sunlight than sulfate. Here we quantify the direct radiative forcing associated with ash and $SO_2$ emissions from these eruptions, including the influence of ash deposition to snow and sea ice. We do not quantify aerosol-cloud indirect forcings, which are extremely complex and difficult to represent in global models [*Stevens and Boucher*, 2012]. We explore uncertainty by considering scenarios of particle optical properties and volcanic emissions that yield low, central, and high direct forcing estimates. We also explore variability in atmospheric forcing across multiple ensemble members.

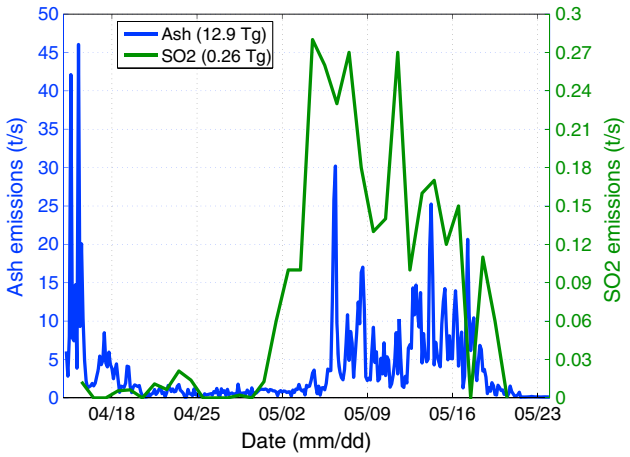


**Figure 1.** Time series of ash and sulfur dioxide ($SO_2$) emissions used to generate central estimates of radiative forcing. Ash emissions are derived by *Stohl et al.* [2011] and represent total mass of particles with radii between 0.125 and 125 μm. May $SO_2$ emissions are derived by *Flemming and Inness* [2013] from GOME-2 measurements, and April emissions are from *Heard et al.* [2012].

## 2. Methods

### 2.1. Aerosol Distributions and Model Setup

We apply the global four-dimensional distributions of atmospheric ash concentrations described by *Stohl et al.* [2011]. These distributions were simulated with the Lagrangian Flexible Particle Dispersion Model (FLEXPART), using an inversion technique that adjusts an a priori ash emission source term to optimize the simulated ash distributions against remote sensing retrievals of ash column loadings. For the purposes of this study, we define "ash" as the mineral particles (tephra) with radii smaller than 125 μm injected into the atmosphere by the eruption. Global ash concentrations and deposition fluxes are provided at daily resolution in 25 size bins with radii ranging from 0.125 to 125 μm, at $1° \times 1°$ horizontal resolution, and in 38 atmospheric layers between the surface and 20 km. The total mass of injected ash in this inventory is 12.9 Tg. Total fine-ash emissions described by *Stohl et al.* [2011] were 8.3 Tg but only accounted for particles with radius ranging from 1.4 to 14 μm. Low and high forcing sensitivity studies (described later) assume ash fields scaled by factors of 0.5 and 2.0, roughly bracketing uncertainty in ash emissions. We apply vertically and temporally resolved May $SO_2$ emissions derived from Global Ozone Monitoring Experiment-2 (GOME-2) measurements [*Flemming and Inness*, 2013] and apply April emissions from *Heard et al.* [2012] to derive a complete time series. Both of these studies find that April $SO_2$ emissions accounted for only a few percent of the total April–May emissions, which are 0.26 Tg in our central scenario. Low estimates are scaled to achieve total May emissions of 0.13 Tg, derived from Scanning Imaging Absorption Spectrometer for Atmospheric Chartography observations [*Flemming and Inness*, 2013], and high estimates are scaled to 0.43 Tg, based on IASI observations [*Heard et al.*, 2012]. Time series of ash and $SO_2$ emission fluxes are displayed in Figure 1, which shows a short period of intense ash emissions in April and a second prolonged eruption episode in May that produced both ash and $SO_2$.

To calculate radiative forcing, we apply the atmosphere (CAM4), land (CLM4), and sea ice (CICE4) components of the Community Earth System Model (CESM) version 1.0.3. All simulations are conducted over the time period 1 January 2009 to 31 December 2010, with 2009 used as a spin-up period and volcanic aerosols imposed in year 2010. Atmospheric simulations provide shortwave (SW) and longwave (LW) radiative forcing of atmospheric ash and sulfate. Sea-surface temperatures and sea ice concentrations from 2009 to 2010, provided by the Hadley Centre [*Rayner et al.*, 2003], are prescribed in these simulations, while the atmospheric state is prognosed by CAM and the land surface state is prognosed by CLM. The atmospheric ash fields from *Stohl et al.* [2011] are prescribed in space and time, after being interpolated to the 26 hybrid sigma pressure levels represented in CAM4 and rebinned into four size bins with radius partitions at 0.5625 μm, 1.0 μm, and 2.5 μm. Each size bin contains roughly equal particle surface area in the global mean, thus optimizing resolution of size-dependent optical properties. We convert ash volume concentrations from *Stohl et al.* [2011] to mass mixing ratios while conserving column burdens. Sulfate aerosols from the volcanic eruptions are prognosed in CAM. Formation of sulfate from $SO_2$ oxidation and aerosol removal through wet and dry processes are simulated with representations from *Rasch et al.* [2000, 2008], using spatially and monthly varying oxidant fields generated from an off-line chemical transport model.

We conduct off-line land model simulations with CLM to calculate shortwave radiative forcing from ash in snow. These simulations are driven with 2009–2010 near-surface air temperatures and atmospheric reanalysis data from the Climate Research Unit and National Centers for Environmental Prediction (NCEP) (ftp://nacp.ornl.gov/synthesis/2009/frescati/model_driver/cru_ncep/analysis/readme.htm). Ash deposition fluxes from *Stohl et al.* [2011], which were also generated with 2010 reanalysis data, are prescribed, and the

vertical distribution of ash in snow is prognosed based on time-dependent precipitation, melt, sublimation, and layer combinations and divisions [*Flanner et al.*, 2007; *Oleson et al.*, 2010]. Melt scavenging ratios are set to 0.02 and 0.01 for the two smaller and larger ash size bins, respectively, identical to values applied for the four dust species that are also used in the model. The melt scavenging ratio is the ratio of the mass concentration of ash in melt water leaving a snow layer to the concentration of ash in the snow layer [*Flanner et al.*, 2007]. A value less than 1 implies that ash becomes more concentrated near the snow surface during melt, as observed by *Conway et al.* [1996]. Similarly, off-line sea ice simulations with CICE are conducted to calculate shortwave radiative forcing by ash in sea ice. These simulations are forced with 2009–2010 atmospheric conditions from NCEP, using the same prescribed ash deposition fields applied in the land simulations. The vertical distribution of ash in overlying snow, underlying sea ice, and exposed sea ice is prognosed using aerosol representations described by *Holland et al.* [2012], with identical melt scavenging ratios and size bins as those used for ash in the land model.

We report averages of the instantaneous top-of-atmosphere radiative forcings for each aerosol component. Atmospheric radiative fluxes are computed with the Rapid Radiative Transfer Model (RRTMG) embedded in CAM [*Iacono et al.*, 2008]. All-sky atmospheric ash and sulfate SW and LW radiative forcings are computed at 1 h resolution from differences in net top-of-atmosphere fluxes calculated with and without each volcanic constituent. Clouds and climatologies of other aerosol constituents—including nonvolcanic sulfate, black and organic carbon, dust, and sea salt—are present in both radiative calculations. Radiative forcing from ash in snow is calculated each 30 min time step at the surface using the Snow, Ice, and Aerosol Radiative (SNICAR) model embedded in CLM [*Flanner et al.*, 2007; *Oleson et al.*, 2010], while surface radiative forcing from ash in sea ice is calculated each time step using the delta-Eddington model embedded in CICE [*Briegleb and Light*, 2007; *Holland et al.*, 2012]. Dust and black carbon are also present in the snow and sea ice forcing calculations. Surface forcings from ash in snow and sea ice are scaled by 0.91 to represent top-of-atmosphere forcing, based on column radiative transfer calculations described by *Flanner et al.* [2007]. The instantaneous radiative forcing employed here differs from the adjusted and effective radiative forcing metrics applied in Intergovernmental Panel on Climate Change assessment reports, which allow, respectively, for the equilibration of stratospheric temperature and rapid adjustments of stratospheric, tropospheric, and land surface states [e.g., *Myhre et al.*, 2013]. *Hansen et al.* [2005] showed, however, that the adjusted and instantaneous forcings of aerosols generally differ by less than 10% (Table 2 of that study). This is true even for Pinatubo aerosols, much of which resided in the stratosphere, though we note that very little of the simulated aerosol burdens from Eyjafjallajökull resided in the stratosphere. This indicates that instantaneous forcing is a reasonable metric to apply for atmospheric aerosol forcing from Eyjafjallajökull. In contrast, light-absorbing aerosols deposited to snow and ice surfaces have been shown to exert an effective forcing several times greater than the instantaneous forcing [*Hansen and Nazarenko*, 2004; *Flanner et al.*, 2007; *Hansen et al.*, 2007; *Myhre et al.*, 2013]. Because the explicit simulations of effective radiative forcing associated with small perturbations, such as those explored here, are hampered by meteorological variability [*Myhre et al.*, 2013], we derive effective forcings simply by scaling the global mean instantaneous forcings by representative efficacy factors derived in previous studies. These effective forcings scale linearly with the expected equilibrium surface temperature responses to the forcings. From *Hansen et al.* [2005], we apply efficacy factors of 1.08 for sulfate and 0.87 for atmospheric ash. The latter is the efficacy reported for soil dust, which we take as a proxy for ash because it absorbs a similar proportion of incident sunlight and consists of large particles that radiate in the longwave. For forcing by ash in snow and sea ice, we assume an efficacy of 3.0, in between values derived from equilibrium [*Flanner et al.*, 2007] and transient [*Hansen et al.*, 2007] climate simulations. The radiative effects of volcanic ash and sulfate do not influence the simulated dynamical state in our simulations. This choice facilitates the simulation of identical climate states in sensitivity studies with varying particle optical properties and mass burdens, allowing us to isolate the impacts of variations in these properties on radiative forcing.

## 3. Aerosol Optical Properties

Optical properties of the ash particles injected from Eyjafjallajökull remain uncertain. Particle optical properties depend on refractive index, size distribution, and shape. We derive spectrally resolved ash properties for each particle size bin by assuming low, central, and high scenarios of the imaginary component of the refractive index ($k$), which governs absorptivity and has a strong bearing on the sign and magnitude of SW

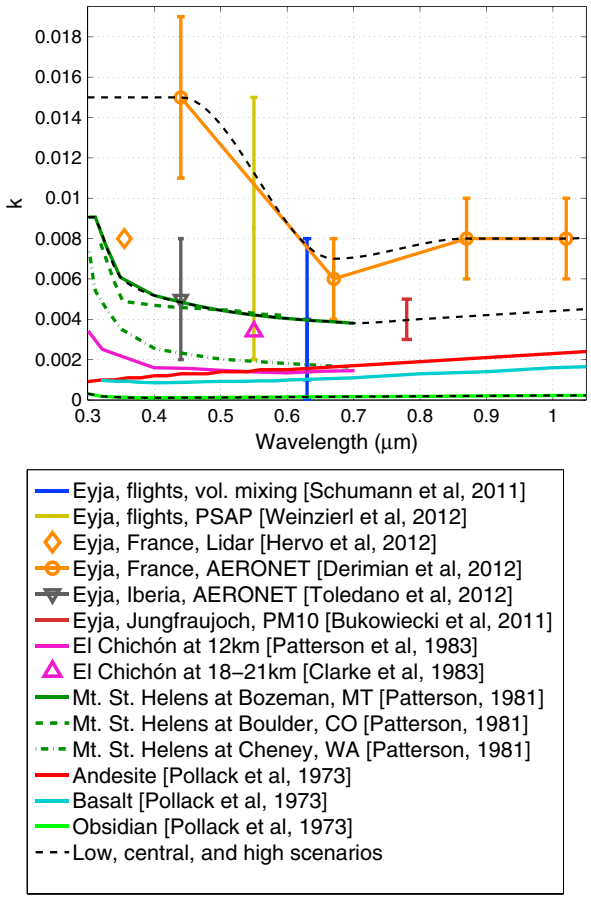


**Figure 2.** Measurements of the imaginary component of the refractive index ($k$) of different ash and volcanic minerals in the solar spectrum. Data labeled "Eyja" (legend) indicate measurements of ash clouds or surface deposits from the Eyjafjallajökull eruptions of 2010. Black dashed lines depict the three scenarios of ash absorptivity applied in forcing sensitivity studies.

forcing from ash. These scenarios are depicted in Figure 2 along with measurements of volcanic minerals, Eyjafjallajökull ash, and ash from other eruptions. In the visible spectrum, estimates of $k$ for Eyjafjallajökull ash range from about 0.001 to 0.015 and are derived from airborne measurements of ash chemical composition and volume mixing assumptions [*Schumann et al.*, 2011], best fit closure between measurements of particulate matter smaller than 10 μm as calculated from ash measurements in air and snow at Jungfraujoch [*Bukowiecki et al.*, 2011], inversions from airborne Particle Soot Absorption Photometer measurements [*Weinzierl et al.*, 2012], inversions from ground-based lidar in central France [*Hervo et al.*, 2012], and inversions of sun photometer measurements from Aerosol Robotic Network (AERONET) sites in France and Spain [*Derimian et al.*, 2012; *Toledano et al.*, 2012] (Figure 2). Measurements of $k$ between wavelengths of 0.3 and 0.7 μm of common volcanic minerals [*Pollack et al.*, 1973], applied in many studies, range from $2.2 \times 10^{-5}$ to 0.0017, whereas $k$ estimates of 1982 El Chichón and 1980 Mount St. Helens ash range from 0.001 to 0.009 [*Patterson*, 1981; *Patterson et al.*, 1983; *Clarke et al.*, 1983].

Our central forcing scenario follows the spectral shape of ash collected from the 1980 Mount St. Helens eruption and is consistent with five independent derivations of Eyjafjallajökull ash $k$ [*Schumann et al.*, 2011; *Bukowiecki et al.*, 2011; *Hervo et al.*, 2012; *Toledano et al.*, 2012; *Weinzierl et al.*, 2012] (Figure 2). Our high scenario is based on the AERONET inversions from *Derimian et al.* [2012] and is within the range of derivations from *Weinzierl et al.* [2012]. Our low scenario follows obsidian measurements [*Pollack et al.*, 1973] and brackets laboratory measurements showing $k$ of ~ 0.001 at 0.7–1.0 μm for fine-ash samples from Eyjafjallajökull [*Helbert et al.*, 2011]. A very recent study applies spectral reflectance measurements of filtered particles to derive visible $k$ of 0.001–0.005 for Eyjafjallajökull ash [*Rocha-Lima et al.*, 2014], in between our low and central scenarios. For the real component of the refractive index we assume a value of 1.54 between 0.2 and 0.55 μm, taken as a mean of visible inversions ranging from 1.50 to 1.60 [*Schumann et al.*, 2011; *Weinzierl et al.*, 2012; *Hervo et al.*, 2012; *Derimian et al.*, 2012] and sloping linearly to 1.47 between 0.55 μm and 5.0 μm following spectral slopes of andesite and basalt [*Pollack et al.*, 1973]. Applying Mie Theory, 0.55 μm single-scatter albedos range from 0.73 to 0.97 for the four particle sizes under the central scenario, from 0.87 to 0.99 under the low scenario, and from 0.60 to 0.93 under the high scenario.

Figure 3 depicts the infrared spectral distribution of the real and imaginary refractive indices of volcanic minerals [*Pollack et al.*, 1973] and ash pumice [*Volz*, 1973]. Also shown are preliminary measurements of Eyjafjallajökull ash samples (D. Peters, personal communication), derived using the method outlined by *Grainger et al.* [2013] for Aso ash. With the exception of *Volz* [1973], these data all show similar peaks in $k$ (absorption) near 9–10 μm and increasing absorption between 12 and 20 μm. The three scenarios of real and imaginary LW refractive indices used here are as follows: (low) data from *Volz* [1973], (central) andesite

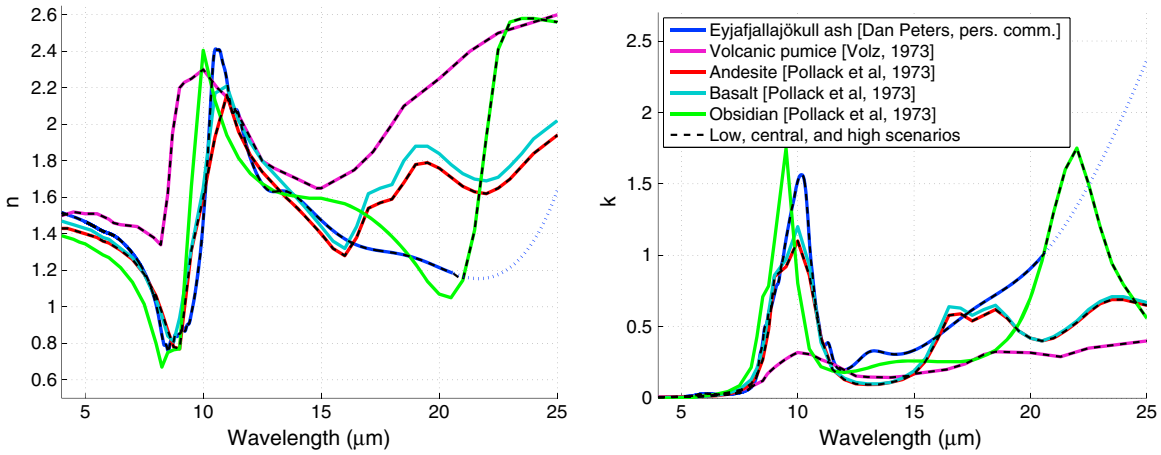


**Figure 3.** Measurements of the (left) real and (right) imaginary components of the refractive index of different ash and volcanic minerals at infrared wavelengths. Black dashed lines depict the three scenarios of ash absorptivity applied in forcing sensitivity studies. The low scenario applies the volcanic pumice data from *Volz* [1973]. The central scenario applies andesite measurements [*Pollack et al.*, 1973]. The high scenario follows measurements of Eyjafjallajökull ash samples from 4 to 21 μm and follows obsidian at wavelengths longer than 21 μm.

measurements [*Pollack et al.*, 1973], and (high) measurements of Eyjafjallajökull ash samples from 4 to 21 μm merged with obsidian at wavelengths longer than 21 μm, owing to uncertainty in the ash measurements at long wavelengths (D. Peters, personal communication).

Sulfate aerosol is essentially nonabsorbing in the SW, and variability in the scattering cross section originates largely from particle size distribution. Our three optical property scenarios assume effective radii (lognormal standard deviations) of 0.17 μm (2.03), 0.27 μm (1.60), and 0.43 μm (1.25). The small and large size distributions are identical to those applied by *Rasch et al.* [2008], representing (respectively) typical tropospheric pollution and stratospheric aerosol measured months following the 1991 eruption of Pinatubo [e.g., *Stenchikov et al.*, 1998]. The central estimate is based on size distributions and sulfate fractions of Eyjafjallajökull aerosol plumes measured at Mace Head station [*O'Dowd et al.*, 2012]. We use refractive indices for sulfate (75% $H_2SO_4$/25% $H_2O$) and relative humidity growth factors from *Hess et al.* [1998], the latter of which are consistent with those measured by *O'Dowd et al.* [2012] for Eyjafjallajökull plumes. These properties are also applied in the LW spectrum, where larger *k* for sulfate allows large particles to contribute to LW forcing.

High spectral resolution (0.01 μm) Mie properties for each scenario are averaged into the 14 SW bands applied in RRTMG, using top-of-atmosphere solar spectral irradiance for sub-band weighting, and are averaged into the 16 LW bands with sub-band weighting according to a 250 K Planck function. All ash optical properties applied here are available as supporting information (Tables S1–S6).

Ash particles are known to be highly aspherical, causing irregularities in the scattering phase functions and bulk optical properties. Microscopic analyses and lidar measurements on Eyjafjallajökull ash indicate irregularly shaped particles with average aspect ratios in the range of 1.8–2.0 [*Ansmann et al.*, 2010; *Gasteiger et al.*, 2011; *Schumann et al.*, 2011; *Weinzierl et al.*, 2012]. We apply *T*-Matrix calculations [*Mishchenko and Travis*, 1998] to explore the potential importance of shape irregularity for radiative forcing. Tables presented in Data S1 list 0.55 μm and 11 μm optical properties of equal-volume spheres, oblate and prolate spheroids with different aspect ratios, and Chebyshev particles. Mass absorption cross sections of these particles differ by at most 16%, with the largest effects associated with small particles in the infrared spectrum, which contribute little to radiative forcing. We conclude that particle shape introduces second-order uncertainty to our direct calculation of radiative forcing, though its impact on remote sensing retrievals that rely on directional scattering is likely larger [e.g., *Kylling et al.*, 2014].

## 4. Aerosol Radiative Forcing

Figures 4 and 5 show the spatial and temporal patterns, respectively, of instantaneous radiative forcing components produced with central estimates of emissions and optical properties. The following features of Eyjafjallajökull aerosol forcing emerge from these figures:

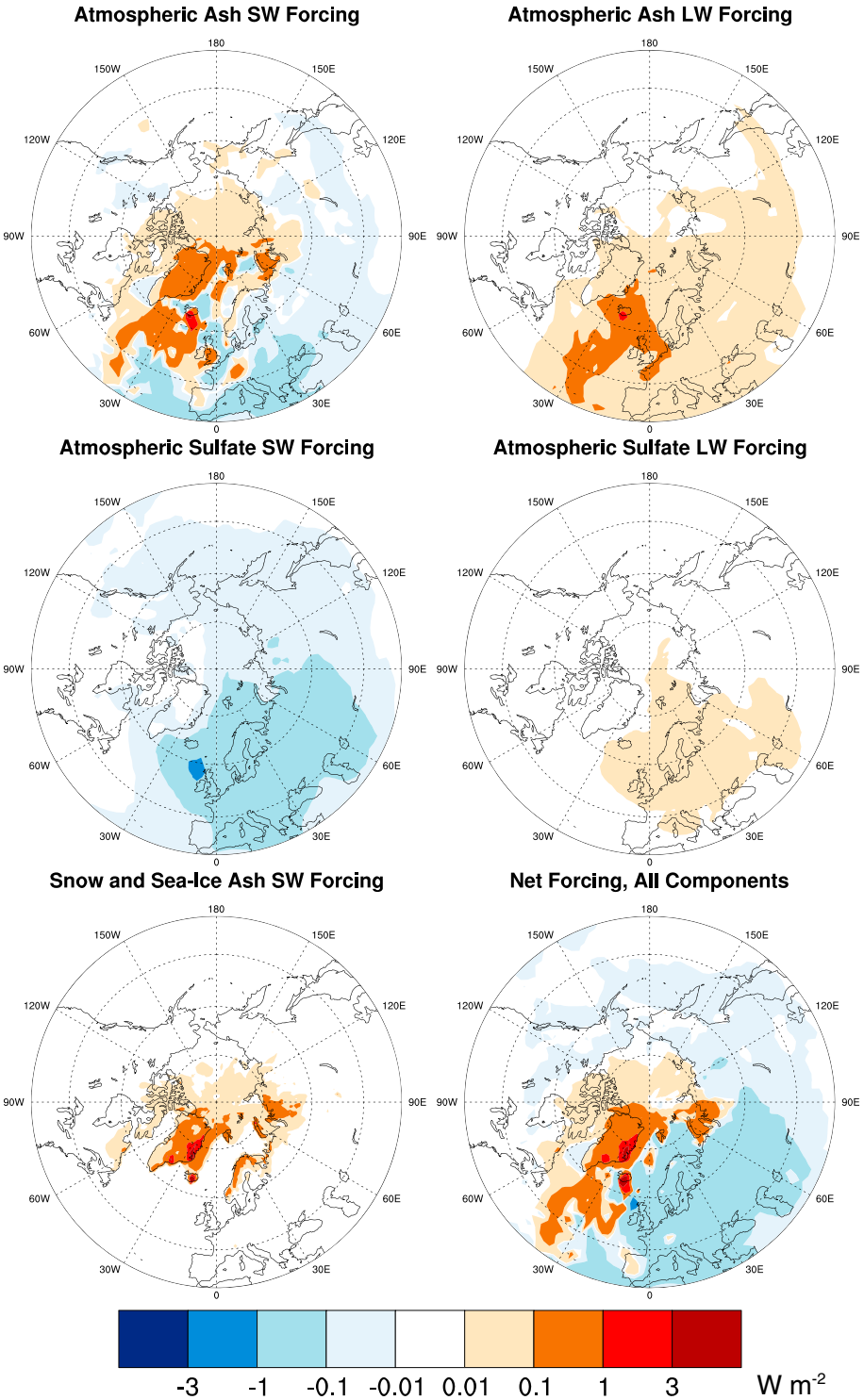


**Figure 4.** Spatial patterns of top-of-atmosphere direct radiative forcing for each component of aerosol forcing, averaged from 14 April to 13 June 2010.

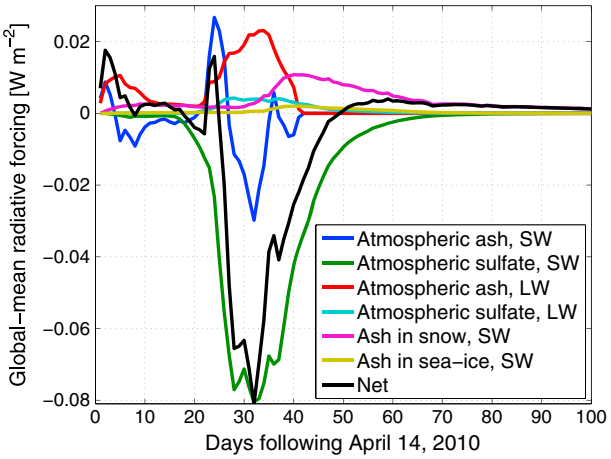


**Figure 5.** Daily global mean top-of-atmosphere direct radiative forcing for each component of aerosol forcing.

1. Both the sign and magnitude of atmospheric ash SW forcing are highly variable, with the sign depending on whether the ash is above reflective surfaces like clouds and snow or over dark surfaces like cloud-free ocean [e.g., *Young et al.*, 2012]. This indicates that the ash SW forcing in this environment is sensitive to both the distribution of clouds and to small differences in visible single-scatter albedo, which in the central scenario of optical properties varies from 0.72 to 0.97 with decreasing particle size.
2. Sulfate is the dominant source of (unambiguously) negative SW forcing, becoming relatively large in mid-May, shortly after the most intense $SO_2$ emission period [*Flemming and Inness*, 2013, Figure 1]. Sulfate forcing also persists longer than ash forcing because of delay in oxidation to $SO_4$ and slower removal time associated with smaller particle size. Very little $SO_2$ was injected into the stratosphere, however, and hence sulfate forcing did not persist for months or years as it does following highly explosive events like Mount Pinatubo. The mass-weighted mean $SO_2$ injection height was 4.5 km, with variations from 2 to 6 km, except on 18 May, when injection reached 9 km [*Flemming and Inness*, 2013]. The April eruption also injected material above 8 km [e.g., *Stohl et al.*, 2011; *Gudmundsson et al.*, 2012] but contained little $SO_2$. As a result, only 0.4% and 3% of the global mean 2010 sulfate and ash burdens, respectively, resided above the tropopause as diagnosed by CAM.
3. Ash deposition on snow and sea ice exerts a positive forcing that can be quite strong locally, especially during the summer solstice season. The global mean forcing is modest, however, because of limited cryospheric coverage. This forcing peaks later and persists much longer than the atmospheric ash forcing because of longer particle retention times in snow and increasing insolation leading up to the solstice. Some of the simulated summer forcing is also caused by melt-induced exposure of buried deposits. Ash deposits in Iceland caused dramatic surface darkening and anomalous melting of local glaciers [*Björnsson et al.*, 2013], though deposits near the vent were sufficiently thick (tens of centimeters) to insulate the snow.
4. LW forcing from atmospheric ash is the largest source of positive radiative forcing during the eruption phase. It is larger than sulfate LW forcing because the ash particles and atmospheric burdens are much larger. As with SW forcing, LW forcing from sulfate persists longer than that of ash. LW forcing of both species is also governed by aerosol altitude and temperature of the radiating environment.
5. The net global mean instantaneous forcing from all components is weakly positive during the April eruption phase, strongly negative during much of May when sulfate SW forcing dominates, and then weakly positive during the rest of the summer when ash deposits continue to darken Arctic snow and ice (Figure 5). Despite small global mean terms, the monthly averaged forcing exceeds $\pm 1$ W m$^{-2}$ in some regions such as eastern Greenland. Animations of daily forcing from each component are provided as supporting information (Animation S1).

Global annual mean forcing components are shown in Table 1. This table also includes results from two sensitivity studies exploring axes of uncertainty space associated with particle optical properties and emissions. In the central scenario (identical for both sets of experiments), atmospheric ash SW forcing is weakly negative but is exceeded by positive LW forcing and SW forcing from deposition to snow and sea ice, yielding net positive ash forcing. Sulfate forcing is strongly negative, however, leading to negative net instantaneous forcing from all components ($-1.9$ mW m$^{-2}$, Table 1). The net effective forcing, which is derived by scaling the instantaneous forcing components by efficacy factors listed in Table 1, is nearly neutral ($-0.5$ mW m$^{-2}$, Table 1) because of amplified positive forcing from ash in snow and sea ice.

The low scenario of optical properties applies higher ash single-scatter albedo (supporting information) and larger sulfate extinction cross section. Atmospheric ash forcing is strongly negative in this case

**Table 1.** Global Annual Mean Radiative Forcings (mW $m^{-2}$)[a]

| | Instantaneous Top-of-Atmosphere Forcings | | | | | | | |
|---|---|---|---|---|---|---|---|---|
| | Ash SW | Ash LW | Ash in Snow | Ash in Sea Ice | Sulfate SW | Sulfate LW | Net Instantaneous | Net Effective[c] |
| *Variable Optical Properties, Central Emissions* | | | | | | | | |
| Low | −4.1 | 0.7 | 0.0 | 0.0 | −4.1 | 0.2 | −7.3 | −7.2 |
| Central[b] | −0.3 | 1.1 | 0.8 | 0.1 | −3.8 | 0.2 | −1.9 | −0.5 |
| High | +2.7 | 1.2 | 1.3 | 0.2 | −3.0 | 0.2 | +2.8 | +4.9 |
| *Variable Emissions, Central Optical Properties* | | | | | | | | |
| Low | −0.1 | 0.5 | 0.4 | 0.1 | −6.1 | 0.4 | −4.9 | −4.3 |
| Central[b] | −0.3 | 1.1 | 0.8 | 0.1 | −3.8 | 0.2 | −1.9 | −0.5 |
| High | −0.6 | 2.1 | 1.5 | 0.3 | −2.1 | 0.1 | +1.2 | +4.5 |

[a]The climate state is identical in each scenario.
[b]Table 2 shows central scenario forcings from ensemble members with perturbed initial conditions.
[c]Effective forcing is derived by scaling the instantaneous forcing with efficacy factors of 0.87 for atmospheric ash, 1.08 for sulfate [*Hansen et al.*, 2005], and 3.0 for ash in snow and sea ice [*Flanner et al.*, 2007; *Hansen et al.*, 2007].

(comparable to sulfate), and ash-in-snow forcing becomes negligible, leading to strongly negative net forcing. In the high optical property scenario, smaller ash single-scatter albedo causes atmospheric ash SW forcing to become positive and drives stronger forcing from ash deposition to snow and sea ice, leading to positive net forcing (Table 1). The range in LW forcing across these simulations is smaller because refractive indices and mass absorption do not change monotonically with scenario in all parts of the spectrum (Figure 3) and also because factors like aerosol altitude strongly influence the relationship between optical properties and LW forcing for a given aerosol mass. The net effective forcing is substantially larger than the instantaneous forcing under the high scenario of optical properties because of large snow and sea ice forcing terms. Conversely, the net instantaneous and effective forcings are very similar under the low scenario of optical properties because cryospheric ash forcing is negligible and efficacy factors for atmospheric aerosols are close to unity.

In a second sensitivity study we scale ash fields down by 50% and $SO_2$ emissions up by 66% for the low forcing scenario and scale ash fields up by 100% and $SO_2$ emissions down by 48% for the high forcing scenario. We apply central estimates of optical properties, which produce positive net ash forcing, and hence this combination of scalings maximizes the low-high forcing range. It is possible for ash and $SO_2$ biases to be of opposite sign because they are derived from radiation measurements in very different parts of the spectrum. (Ash was derived from infrared measurements [*Stohl et al.*, 2011] and $SO_2$ from ultraviolet measurements [*Flemming and Inness*, 2013].) Each component of global mean forcing scales roughly linearly with these changes. Net forcing becomes less positive for ash and more negative for sulfate in the low scenario and vice versa in the high scenario. The low-high range in total forcing is smaller in this set of experiments than with variable optical properties. This is partially a consequence of compensating SW and LW forcing components from each constituent. The choice of emissions scalings, however, is somewhat subjective. *Stohl et al.* [2011] estimate uncertainty in their ash fields to be 50%, which is consistent with subsequent evaluations of these fields against observations [*Schumann et al.*, 2011; *Hervo et al.*, 2012; *Toledano et al.*, 2012]. *Gudmundsson et al.* [2012] estimate total fine-ash emissions several times larger than *Stohl et al.* [2011], though these include a substantial amount of ash that deposited quickly in the vicinity of the volcano. The range in $SO_2$ emissions spans the range of remote sensing retrievals derived from four different instruments [*Flemming and Inness*, 2013; *Heard et al.*, 2012]. Additional uncertainty in sulfate forcing arises from the oxidation rates of $SO_2$ and removal rates of sulfate aerosol, which we do not assess here.

We explore a third dimension of uncertainty associated with variability in the distribution of clouds. As noted earlier, atmospheric ash SW forcing is highly sensitive to clouds. Under assumptions of moderately or strongly absorbing ash (central and high optical property scenarios), the presence of clouds often reverses the sign of ash forcing in regions not covered with snow or ice. Clouds also decrease the absolute

**Table 2.** Global Annual Mean Instantaneous Top-of-Atmosphere Radiative Forcings From Different Ensemble Members (mW m$^{-2}$)

| Ensemble Member | Ash SW | Ash LW | Sulfate SW | Sulfate LW |
|---|---|---|---|---|
| E1[a] | −0.29 | 1.06 | −3.83 | 0.24 |
| E2 | −0.59 | 1.07 | −3.73 | 0.24 |
| E3 | −0.45 | 1.03 | −3.56 | 0.22 |
| E4 | −0.20 | 1.07 | −3.62 | 0.22 |
| E5 | −0.28 | 1.05 | −3.57 | 0.22 |
| Mean | −0.36 | 1.06 | −3.66 | 0.23 |

[a]Ensemble member E1 represents the central scenario shown in Table 1 and Figures 4 and 5.

magnitude of sulfate SW forcing by decreasing available insolation. We conduct four additional simulations of the central scenario of atmospheric forcing, each with slightly perturbed initial conditions. All simulations apply identical sea-surface temperatures, but the meteorology is subject to chaotic variation. Forcings from each of these ensemble members are summarized in Table 2. Except for atmospheric ash SW forcing, the variations across all ensemble members are less than 5% of the ensemble mean. The atmospheric ash SW forcing, however, ranges from −0.20 to −0.59 mW m$^{-2}$ across ensemble members, indicating that variations in the spatial relationship between clouds and the ash plumes can substantially impact the ash global mean instantaneous forcing. The central estimate of net instantaneous forcing (Table 1) shifts only from −1.9 to −1.8 mW m$^{-2}$ when ensemble mean atmospheric forcing terms are applied.

Finally, a recent study shows that temporal inconsistencies between prescribed precipitation and aerosol deposition fluxes in off-line CLM simulations, such as those applied here, can lead to high biases of about a factor of 2 in the simulated concentrations of particles in the surface snow layer [*Doherty et al.*, 2014]. It follows that radiative forcing estimates would also be biased high. These biases are likely mitigated in the current study, however, because (1) the meteorological fields used to simulate the ash deposition fluxes [*Stohl et al.*, 2011] and to drive the CLM simulations both originated from 2010 reanalysis data, and thus precipitation and wet deposition fluxes are consistent with each other and (2) a substantial portion of the ash was deposited through dry processes, especially in cryospheric regions near the volcanic source.

## 5. Concluding Discussion

We provide the first estimates of global aerosol radiative forcing from the Eyjafjallajökull eruptions of 2010. Global mean direct instantaneous forcing for 2010 is estimated at −1.9 (−7.3 to +2.8) mW m$^{-2}$, with uncertainty arising from particle optical properties and emissions of ash and $SO_2$. Net effective forcing of −0.5 (−7.2 to +4.9) mW m$^{-2}$ is slightly larger due to high efficacy of ash deposition to snow and sea ice. Shortwave forcing from atmospheric ash is weakly negative under our central estimates of optical properties, which are derived from various measurements of Eyjafjallajökull and other ash. Negative forcing from sulfate slightly exceeds the combined positive forcings from ash deposition to snow and longwave absorption by atmospheric ash and sulfate, though we cannot rule out a positive net aerosol forcing from this event. Additional uncertainty arises from aerosol-cloud indirect and semidirect effects, which are extremely difficult to represent in high-latitude regions where thin and mixed-phase clouds prevail [e.g., *Alterskjær et al.*, 2010; *Jacobson*, 2010]. Air sampling over Germany and Israel provides strong evidence that Eyjafjallajökull ash served as ice nuclei [*Bingemer et al.*, 2012]. Previous work suggests that the sign of net cloud forcing associated with black carbon is uncertain but likely positive [*Bond et al.*, 2013], offering a possible analog for the light-absorbing ash component of volcanic emissions, while indirect cloud forcing from $SO_2$ emissions is very likely negative. Net warming from volcanic aerosol emissions would mark an unusual (if small) source of warming in present climate, though this study implies that volcanic aerosols were much more likely to have warmed past climates with larger glaciated area. Each forcing component operates on different time scales, with ash-in-snow and sulfate forcing persisting longer than atmospheric ash forcing, which diminishes quickly as large particles deposit from the atmosphere. The spatial pattern of forcing (Figure 4) may also have important climate ramifications, even if global mean forcing is near climate neutral. For example, persistent darkening of Greenland snow and Arctic sea ice by ash has potential to drive sea level rise and albedo feedback, and the latitudinal gradient in atmospheric forcing could reduce the temperature contrast between the subtropics and Arctic, implying a possible weakening of westerly winds. The complexity of radiative forcing from volcanic ash and its potential to alter high-latitude climate warrant further investigation.

**Acknowledgments**
We thank Daniel Peters and Don Grainger (University of Oxford) for providing us with optical property measurements of ash samples. We also thank two anonymous reviewers for providing very helpful comments. Ash optical data created for our forcing calculations are available as supporting information. Source code for CESM 1.0.3 is available through http://www2.cesm.ucar.edu/. This work was partially supported by NSF ARC-1253154.

## References

Abbot, D. S., and R. T. Pierrehumbert (2010), Mudball: Surface dust and snowball Earth deglaciation, *J. Geophys. Res.*, *115*, D03104, doi:10.1029/2009JD012007.

Alterskjær, K., J. E. Kristjánsson, and C. Hoose (2010), Do anthropogenic aerosols enhance or suppress the surface cloud forcing in the Arctic?, *J. Geophys. Res*, *115*, D22204, doi:10.1029/2010JD014015.

Ansmann, A., et al. (2010), The 16 April 2010 major volcanic ash plume over central Europe: EARLINET lidar and AERONET photometer observations at Leipzig and Munich, Germany, *Geophys. Res. Lett.*, *37*, L13810, doi:10.1029/2010GL043809.

Bingemer, H., et al. (2012), Atmospheric ice nuclei in the Eyjafjallajökull volcanic ash plume, *Atmos. Chem. Phys.*, *12*(2), 857–867, doi:10.5194/acp-12-857-2012.

Björnsson, H., F. Pálsson, S. Gudmundsson, E. Magnússon, G. Adalgeirsdóttir, T. Jóhannesson, E. Berthier, O. Sigurdsson, and T. Thorsteinsson (2013), Contribution of Icelandic ice caps to sea level rise: Trends and variability since the Little Ice Age, *Geophys. Res. Lett.*, *40*(8), 1546–1550, doi:10.1002/grl.50278.

Bond, T. C., et al. (2013), Bounding the role of black carbon in the climate system: A scientific assessment, *J. Geophys. Res. Atmos.*, *118*, 5380–5552, doi:10.1002/jgrd.50171.

Briegleb, B. P., and B. Light (2007), A Delta-Eddington multiple scattering parameterization for solar radiation in the sea ice component of the Community Climate System Model, *Tech. Rep. NCAR/TN–472+STR*, Natl. Cent. for Atmos. Res., Boulder, Colo.

Bukowiecki, N., et al. (2011), Ground-based and airborne in-situ measurements of the Eyjafjallajökull volcanic aerosol plume in Switzerland in spring 2010, *Atmos. Chem. Phys.*, *11*(19), 10,011–10,030, doi:10.5194/acp-11-10011-2011.

Clarke, A. D., R. J. Charlson, and J. A. Ogren (1983), Stratospheric aerosol light absorption before and after El Chichon, *Geophys. Res. Lett.*, *10*(11), 1017–1020, doi:10.1029/GL010i011p01017.

Conway, H., A. Gades, and C. F. Raymond (1996), Albedo of dirty snow during conditions of melt, *Water Resour. Res.*, *32*(6), 1713–1718.

Derimian, Y., O. Dubovik, D. Tanre, P. Goloub, T. Lapyonok, and A. Mortier (2012), Optical properties and radiative forcing of the Eyjafjallajökull volcanic ash layer observed over Lille, France, in 2010, *J. Geophys. Res.*, *117*, D00U25, doi:10.1029/2011JD016815.

Doherty, S. J., C. M. Bitz, and M. G. Flanner (2014), Biases in modeled surface snow BC mixing ratios in prescribed aerosol climate model runs, *Atmos. Chem. Phys. Discuss.*, *14*(9), 13,167–13,196, doi:10.5194/acpd-14-13167-2014.

Flanner, M. G., C. S. Zender, J. T. Randerson, and P. J. Rasch (2007), Present-day climate forcing and response from black carbon in snow, *J. Geophys. Res.*, *112*, D11202, doi:10.1029/2006JD008003.

Flemming, J., and A. Inness (2013), Volcanic sulfur dioxide plume forecasts based on UV satellite retrievals for the 2011 Grimsvötn and the 2010 Eyjafjallajökull eruption, *J. Geophys. Res. Atmos.*, *118*, 10,172–10,189, doi:10.1002/jgrd.50753.

Gasteiger, J., S. Groß, V. Freudenthaler, and M. Wiegner (2011), Volcanic ash from Iceland over Munich: Mass concentration retrieved from ground-based remote sensing measurements, *Atmos. Chem. Phys.*, *11*(5), 2209–2223, doi:10.5194/acp-11-2209-2011.

Grainger, R. G., D. M. Peters, G. E. Thomas, A. J. A. Smith, R. Siddans, E. Carboni, and A. Dudhia (2013), Measuring volcanic plume and ash properties from space, in *Remote Sensing of Volcanoes and Volcanic Processes: Integrating Observation and Modelling*, edited by D. Pyle and T. Mather, *Geol. Soc. London Spec. Publ.*, *380*, 293–320.

Gudmundsson, M. T., et al. (2012), Ash generation and distribution from the April–May 2010 eruption of Eyjafjallajökull, Iceland, *Sci. Rep.*, *2*, 572, doi:10.1038/srep00572.

Hansen, J., and L. Nazarenko (2004), Soot climate forcing via snow and ice albedos, *Proc. Natl. Acad. Sci.*, *101*(2), 423–428.

Hansen, J., et al. (2005), Efficacy of climate forcings, *J. Geophys. Res.*, *110*, D18104, doi:10.1029/2005JD005776.

Hansen, J., et al. (2007), Climate simulations for 1880–2003 with GISS modelE, *Clim. Dyn.*, *29*, 661–696, doi:10.1007/s00382-007-0255-8.

Heard, I. P. C., A. J. Manning, J. M. Haywood, C. Witham, A. Redington, A. Jones, L. Clarisse, and A. Bourassa (2012), A comparison of atmospheric dispersion model predictions with observations of $SO_2$ and sulphate aerosol from volcanic eruptions, *J. Geophys. Res.*, *117*, D00U22, doi:10.1029/2011JD016791.

Helbert, J., A. Maturilli, T. Roush, and H. Mannstein (2011), Deriving optical constants of volcanish ash using measurements from the planetary emissivity laboratory at DLR, in *Hyperspectral Image and Signal Processing: Evolution in Remote Sensing (WHISPERS), 2011 3rd Workshop on*, pp. 1–5, IEEE, Lisbon, Portugal, doi:10.1109/WHISPERS.2011.6080907.

Hervo, M., et al. (2012), Physical and optical properties of 2010 Eyjafjallajökull volcanic eruption aerosol: Ground-based, lidar and airborne measurements in France, *Atmos. Chem. Phys.*, *12*(4), 1721–1736, doi:10.5194/acp-12-1721-2012.

Hess, M., P. Koepke, and I. Schult (1998), Optical properties of aerosols and clouds: The software package OPAC, *Bull. Am. Meteorol. Soc.*, *79*(5), 831–844.

Holland, M., D. A. Bailey, B. P. Briegleb, B. Light, and E. Hunke (2012), Improved sea ice shortwave radiation physics in CCSM4: The impact of melt ponds and aerosols on Arctic sea ice, *J. Clim.*, *25*, 1413–1430, doi:10.1175/JCLI-D-11-00078.1.

Iacono, M. J., J. S. Delamere, E. J. Mlawer, M. W. Shephard, S. A. Clough, and W. D. Collins (2008), Radiative forcing by long-lived greenhouse gases: Calculations with the AER radiative transfer models, *J. Geophys. Res.*, *113*, D13103, doi:10.1029/2008JD009944.

Jacobson, M. Z. (2010), Short-term effects of controlling fossil-fuel soot, biofuel soot and gases, and methane on climate, Arctic ice, and air pollution health, *J. Geophys. Res.*, *115*, D14209, doi:10.1029/2009JD013795.

Kylling, A., M. Kahnert, H. Lindqvist, and T. Nousiainen (2014), Volcanic ash infrared signature: Porous non-spherical ash particle shapes compared to homogeneous spherical ash particles, *Atmos. Meas. Tech.*, *7*(4), 919–929, doi:10.5194/amt-7-919-2014.

Le Hir, G., Y. Donnadieu, G. Krinner, and G. Ramstein (2010), Toward the snowball Earth deglaciation..., *Clim. Dyn.*, *35*(2–3), 285–297, doi:10.1007/s00382-010-0748-8.

Mishchenko, M. I., and L. D. Travis (1998), Capabilities and limitations of a current FORTRAN implementation of the T-matrix method for randomly oriented, rotationally symmetric scatterers, *J. Quant. Spectrosc. Radiat. Transfer*, *60*(3), 309–324.

Myhre, G., et al. (2013), Anthropogenic and natural radiative forcing, in *Climate Change 2013: The Physical Science Basis. Contribution of Working Group I to the Fifth Assessment Report of the Intergovernmental Panel on Climate Change*, edited by T. F. Stocker et al., pp. 659–740, Cambridge Univ. Press, Cambridge, U. K., and New York.

O'Dowd, C., et al. (2012), The Eyjafjallajökull ash plume—Part I: Physical, chemical and optical characteristics, *Atmos. Environ.*, *48*, 129–142, doi:10.1016/j.atmosenv.2011.07.004.

Oleson, K. W., et al. (2010), Technical description of version 4.0 of the Community Land Model (CLM), *Tech. Rep. NCAR/TN–478+STR*, Natl. Cent. for Atmos. Res., Boulder, Colo.

Patterson, E. M. (1981), Measurements of the imaginary part of the refractive index between 300 and 700 nanometers for Mount St. Helens ash, *Science*, *211*(4484), 836–838.

Patterson, E. M., C. O. Pollard, and I. Galindo (1983), Optical properties of the ash from El Chichon Volcano, *Geophys. Res. Lett.*, *10*(4), 317–320, doi:10.1029/GL010i004p00317.

Pollack, J. B., O. B. Toon, and B. K. Khare (1973), Optical properties of some terrestrial rocks and glasses, *Icarus*, *19*, 372–389.
Rasch, P. J., M. C. Barth, J. T. Kiehl, S. E. Schwartz, and C. M. Benkovitz (2000), A description of the global sulfur cycle and its controlling processes in the National Center for Atmospheric Research Community Climate Model, *J. Geophys. Res.*, *105*, 1367–1385.
Rasch, P. J., P. J. Crutzen, and D. B. Coleman (2008), Exploring the geoengineering of climate using stratospheric sulfate aerosols: The role of particle size, *Geophys. Res. Lett.*, *35*, L02809, doi:10.1029/2007GL032179.
Rayner, N. A., D. E. Parker, E. B. Horton, C. K. Folland, L. V. Alexander, D. P. Rowell, E. C. Kent, and A. Kaplan (2003), Global analysis of sea surface temperature, sea ice, and night marine air temperature since the late 19th century, *J. Geophys. Res.*, *108*(D14), 4407, doi:10.1029/2002JD002670.
Robock, A. (2000), Volcanic eruptions and climate, *Rev. Geophys.*, *38*(2), 198–219, doi:10.1029/1998RG000054.
Robock, A. (2013), The latest on volcanic eruptions and climate, *Eos Trans. AGU*, *94*(35), 305–306, doi:10.1002/2013EO350001.
Rocha-Lima, A., J. V. Martins, L. A. Remer, N. A. Krotkov, M. H. Tabacniks, Y. Ben-Ami, and P. Artaxo (2014), Optical, microphysical and compositional properties of the Eyjafjallajökull volcanic ash, *Atmos. Chem. Phys. Discuss.*, *14*(9), 13,271–13,300, doi:10.5194/acpd-14-13271-2014.
Schumann, U., et al. (2011), Airborne observations of the Eyjafjalla volcano ash cloud over Europe during air space closure in April and May 2010, *Atmos. Chem. Phys.*, *11*(5), 2245–2279, doi:10.5194/acp-11-2245-2011.
Stenchikov, G. L., I. Kirchner, A. Robock, H. F. Graf, J. C. Antuña, R. G. Grainger, A. Lambert, and L. Thomason (1998), Radiative forcing from the 1991 Mount Pinatubo volcanic eruption, *J. Geophys. Res.*, *103*(D12), 13,837–13,857.
Stevens, B., and O. Boucher (2012), Climate science: The aerosol effect, *Nature*, *490*(7418), 40–41, doi:10.1038/490040a.
Stohl, A. et al. (2011), Determination of time- and height-resolved volcanic ash emissions and their use for quantitative ash dispersion modeling: The 2010 Eyjafjallajökull eruption, *Atmos. Chem. Phys.*, *11*(9), 4333–4351, doi:10.5194/acp-11-4333-2011.
Toledano, C., et al. (2012), Aerosol properties of the Eyjafjallajökull ash derived from sun photometer and satellite observations over the Iberian Peninsula, *Atmos. Environ.*, *48*, 22–32, doi:10.1016/j.atmosenv.2011.09.072.
Volz, F. E. (1973), Infrared optical constants of ammonium sulfate, Saharan dust, volcanic pumice, and flyash, *Appl. Opt.*, *12*(3), 564–568.
Weinzierl, B., et al. (2012), On the visibility of airborne volcanic ash and mineral dust from the pilot's perspective in flight, *Phys. Chem. Earth*, *45–46*, 87–102, doi:10.1016/j.pce.2012.04.003.
Young, C. L., I. N. Sokolik, and J. Dufek (2012), Regional radiative impact of volcanic aerosol from the 2009 eruption of Mt. Redoubt, *Atmos. Chem. Phys.*, *12*(8), 3699–3715, doi:10.5194/acp-12-3699-2012.